Mechanically Cutting Organic Single-Crystal Films

Hui-Yao Lin[1], Fei Tong[1]*, Chengyuan Yu[1], Le Li[1], Ben L. Feringa[1,2]*, Da-Hui Qu[1]*

1. Key Laboratory for Advanced Materials and Joint International Research Laboratory of Precision Chemistry and Molecular Engineering,
Feringa Nobel Prize Scientist Joint Research Center,
Frontiers Science Center for Materiobiology and Dynamic Chemistry,
Institute of Fine Chemicals,
School of Chemistry and Molecular Engineering,
East China University of Science and Technology,
130 Meilong Road, Shanghai, 200237 (China)
2. Stratingh Institute for Chemistry and Zernike Institute for Advanced Materials,
University of Groningen,
Nijenborgh 4, 9747 AG Groningen (Netherlands)
Emails of Corresponding Authors:
feitong@ecust.edu.cn
b.l.feringa@rug.nl
dahui_qu@ecust.edu.cn

Abstract: **Most organic molecular crystals exhibit brittleness and are prone to fragmentation when subjected to even mild mechanical forces. Here we reported one new top-down strategy using ordinary scissors to cut for the desired and precise shapes like semicircles, triangles, and pentagons with retention of macroscopic integrity. This unconventional yet simple shape editing approach leverages the chiral asymmetry effect and the steric effect, leading to high asymmetry and enhanced energy dissipation capability during the shear force-driven lattice slippage process. These resulting bulk crystals exhibit good elasticity and allow for photo-induced single-crystal-to-single-crystal (SCSC) modulus enhancement through molecular rearrangement for improved symmetry. Within a broader perspective, this study highlights the strategic integration of top-down and bottom-up approaches, rendering the organic molecular crystals with desirable anisotropic properties and enabling their precise and straightforward further processability.**

The structural characteristics of pure organic crystals, involving high hardness, brittleness, and fragility, have an uncoordinated trade-off with the processing and fabrication at the macroscopic scale. Over the recent decades, top-down material fabricating techniques, such as lithography,[1–3] mechanical grinding,[4,5] and laser ablation,[6–8] have offered high spatiotemporal precision at multiple scales, emerging prominently in materials manufacturing, processing, refining, and functionality.[9–14] Nevertheless, preparing specific habits (morphology, shape, or size) in a single crystal composed of pure organic components is still challenging because a crystal is fragile to fatigue and disintegrate upon mild mechanical forces.[15,16] Bottom-up strategies allow for controlling the composition, structure, and orientation at the molecular or atomic level,[17–19] thereby achieving desirable peculiarities and customized properties like elastic and plastic crystals.[20,21] However, one must extricate from the predicament caused by the inherent molecular variability (intermolecular interactions, molecular configurations, and rigidity) in making desirable materials.

Herein, we describe a simple top-down approach to shaping desirable organic single crystals on-demand based on a chiral 1,2-dithiolane derivative (***R*-TAE**). Macroscopic ***R*-TAE** single crystal thin films (Supplementary Figs. 2-3), grown by a non-classic solvent diffusion method, can be mechanically cut by ordinary scissors. The cropping patterns can be arbitrarily chosen and programmed into circles, continuous waves, well-defined triangles, and irregular pentagons (Fig. 1a and Supplementary Fig. 4). The super-elastic ***R*-TAE** crystalline films possess a lamellar molecular stacking structure connected by a two-dimensional (2D) zig-zag hydrogen bonds network. The crystallinity and structural integrity are perfectly preserved with smooth-cropped realms, showing no sign of chemical transformation, physical phase transition, or cracking after cutting. We deduce that the long-range directionality of the five-membered disulfide ring containing the solely chiral carbon atom, which allows a broken-symmetry effect that accommodates the dynamic slippage between hydrogen bond network inside the crystal lattice, would account for the efficient energy dissipation and molecular sliding during cutting. Compared to racemic crystals consisting of both *R*- and *S*-configuration isomers (***RS*-TAE**), experimental and computational results of the internal cohesive energy of the chiral ***R*-TAE** crystals reveal that energy dissipation is more efficient, enabling the crystal to relax to a more stable state upon external shear force and stress. A shear-force model based on intermolecular interactions and ***R*-TAE** single crystal structure was proposed to elucidate the molecular sliding and energy dissipation process. Before the strategy shown in Fig. 1a, it is essential to investigate how the ***R*-TAE** single crystals form and act at the molecular level, as explained below.

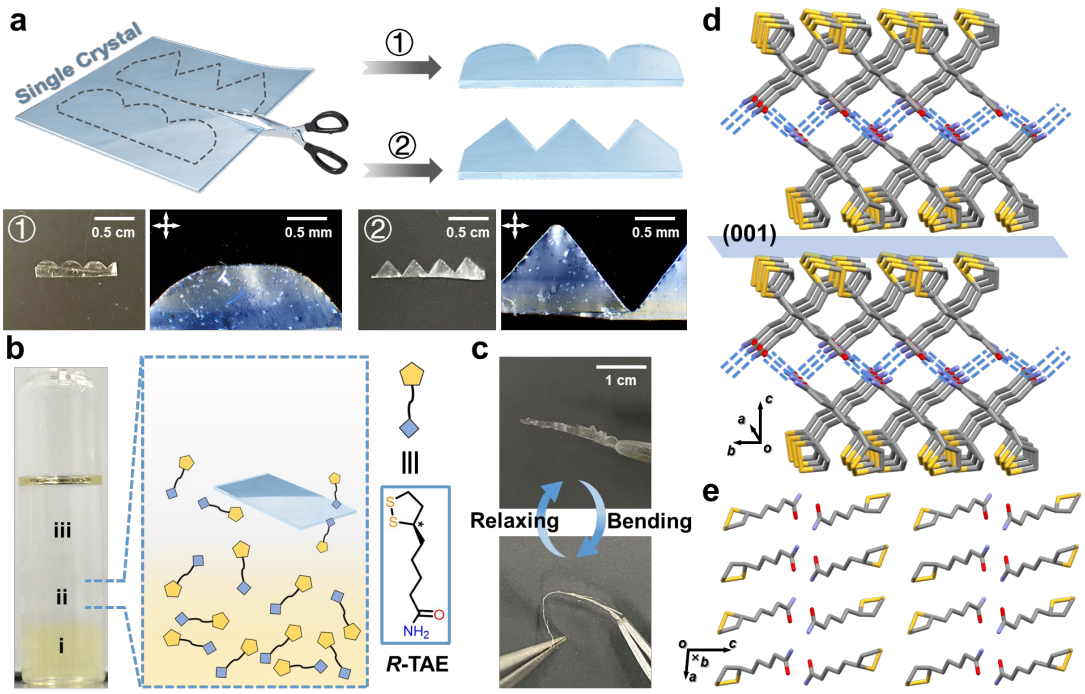

Figure 1. The mechanical cutting properties and growth conditions of *R*-TAE single-crystal thin films. a, Cartoon diagrams of cropping crystals by ordinary scissors, and optical and cross-polarized microscope images of the obtained shapes: 1. Semicircular waves and 2. Rigid triangular waves. **b,** Schematic diagrams of ***R*-TAE** single crystals prepared in three-phase solution (i, ii, and iii represent chloroform, dichloromethane, and cyclohexane). **c,** A macroscopic ***R*-TAE** single crystal plate displays cyclic curling and uncurling under external stress. **d-e,** The single crystal structure of ***R*-TAE** with the 2D zig-zag hydrogen network, viewed along the plane of (001) Miller index and the crystallographic *b*-axis. Sulfur, carbon, oxygen, and nitrogen atoms are shown in yellow, grey, red, and blue, respectively. The hydrogen bonds are shown in the blue dashed line. Hydrogen atoms have been omitted for clarity.

Distinct from most elastic molecular crystals in slender shape, the ***R*-TAE** single crystals prepared by a three-phase solvent diffusion method with optimized solvent ratios are sheet-like, adopting a thin film morphology (Fig. 1b and Supplementary Fig. 5). The prepared crystals can dramatically bend and curl with high curvature under external stress and fully recover after the force is removed, which can be repeated in multiple cycles (>100) (Fig. 1c, Supplementary Fig. 6, and Video 1). The combination of cyclic disulfides with short alkyl chains through a sole chiral carbon atom not only imparts molecular flexibility but also, ascribed to the presence of larger atomic radius sulfur atoms and the interior strains of the five-membered rings, provides a steric effect that significantly influences the molecular packing motif. Besides, the NH_2 group bestows more hydrogen bonding sites through side-chain engineering, thereby

cooperatively enhancing the directionality of molecular arrangement within the crystal lattice. The single-crystal X-ray diffraction characterization (SCXRD) shows that the ***R*-TAE** crystal crystallized in one of the *Sohncke* space groups ($P2_1$) that lacks symmetry elements.[22,23] Moreover, paired ***R*-TAE** molecules adopt a head-to-head packing motif along the plane of (001) Miller index, forming a lamellar stacking structure linked by the zig-zag 2D hydrogen bonds. The interlayer disulfide rings have the same orientation (all facing left in Fig. 1d) and are connected head-to-head by dispersion force (Fig. 1e).

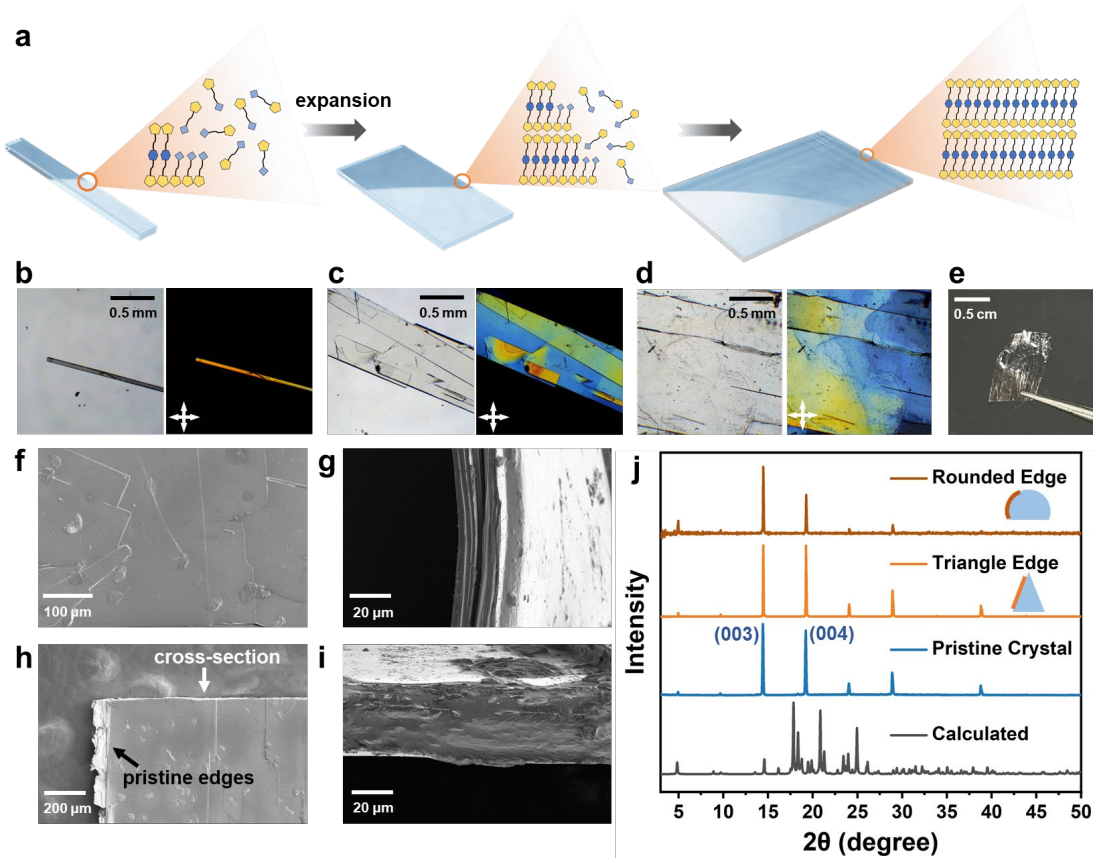

Figure 2. The process of crystal growth expansion and cross-sectional characteristics. a, Cartoon diagrams of the crystal growth expansion process while **b-d** shows the associated optical and polarizing microscope images. **e,** The snapshot of a plate-like ***R*-TAE** single crystal. **f-g,** Scanning electron microscope (SEM) images of the layered structure of the crystals. **h-i,** SEM images of the shear planes with cross-section and pristine edges. **j.** Stacked XRD patterns of the rounded and triangle edges (Micro-XRD) with pristine crystals and calculated pattern.

Fig. 2a displays the details of a multi-stage crystal growing process of macroscopic ***R*-TAE** single crystals. ***R*-TAE** molecules first assemble into crystalline needles. The formation of primary amide hydrogen bonds requires one molecule to connect with the

other three from the surroundings, leading ***R*-TAE** molecules to spontaneously stack in space and allowing needles to grow further (Supplementary Fig. 7). The non-parallel and unequal distances between atoms in a hydrogen bond indicate a degree of symmetry loss in the crystal lattice, making it less susceptible to external disturbances and defects and facilitating the crystal growth to the macroscopic dimensions. Optical and cross-polarized microscope characterization showed the morphology evolutions of an ***R*-TAE** crystal at different stages, verifying that high crystallinity was established during the crystal growth (Figs. 2b-c). After incubation and expansion, plain single crystals on a centimeter scale were harvested (Figs. 2d-e). Scanning electron microscope (SEM) and Transmission Electron Microscope (TEM) images reveal their surfaces are smooth and flat, with distinct layered structures (Figs. 2f-g and Supplementary Fig. 8). After mechanically cutting with scissors, the cross-section at the cut region is smooth and even. The interior molecular stackings are also perfectly preserved after cutting, showing an apparent lamellar structure. The cut region is distinctively different from the interfaces caused by crystal disintegration or tearing, which would cause random edges and sides (Figs. 2h-i). The results are also consistent with the micro-beam single crystal X-ray diffraction (Micro-XRD) characterization, which shows no shifts of molecular packing at the cutting region compared to an intact pristine ***R*-TAE** crystal (Fig. 2j).

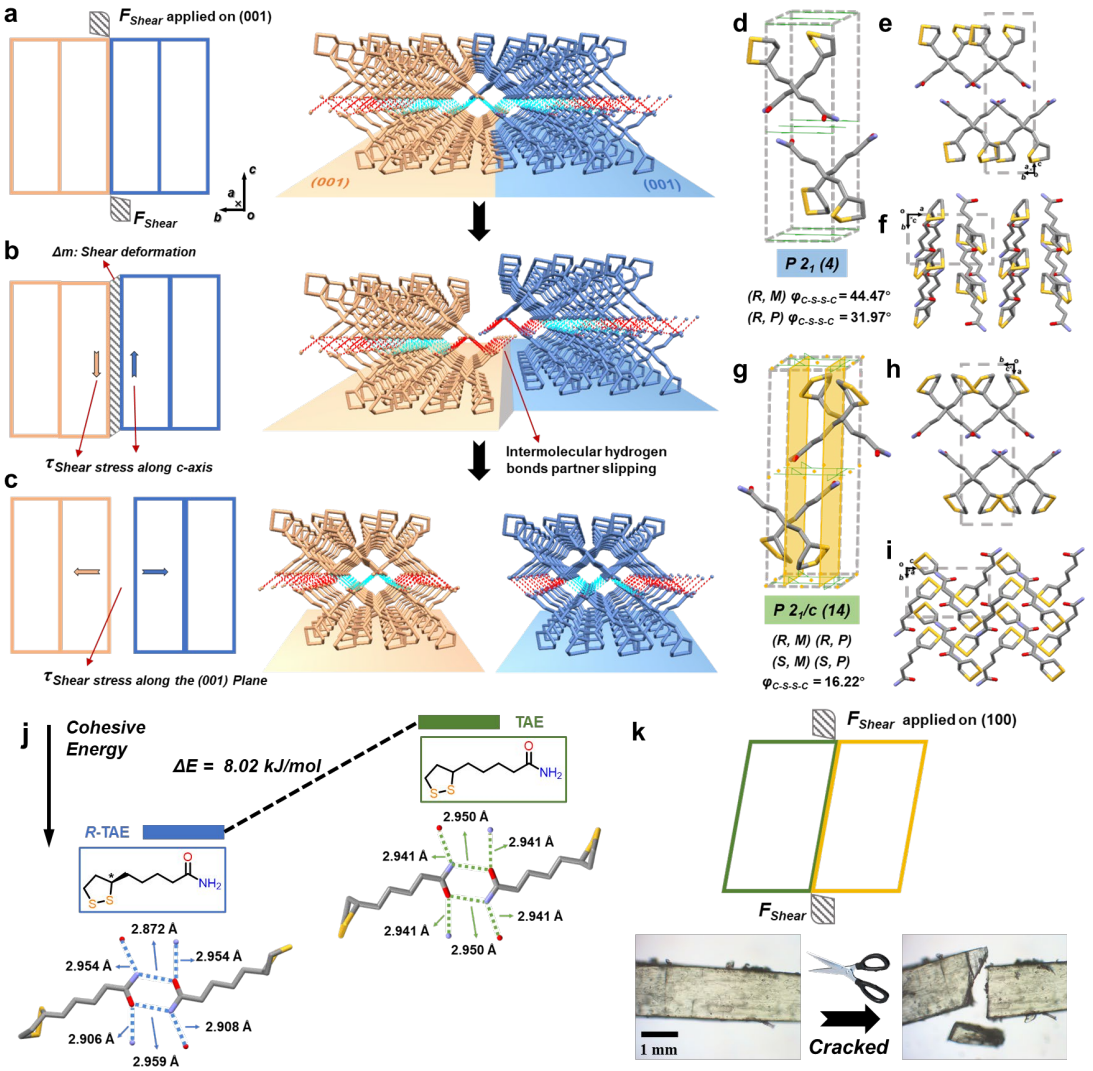

Figure 3. Schematic representation of the shear deformation model of single crystals and the comparison at different levels of structural hierarchy between single enantiomer and racemic molecules. a-c, Proposed shear deformation models of crystalline lattices and their schematic diagrams. The hydrogen bonds are shown in blue and red dashed lines. **d-f,** The 3D crystal lattice and the views along the crystallographic *a* and *c* axes of the ***R*-TAE** single crystal. **g-i,** The 3D crystal lattice and the views along the crystallographic *a* and *c* axes of the ***RS*-TAE** single crystal. Yellow parallelograms represent symmetry planes in the crystal lattice. **j,** The difference of crystal cohesive energy and the atomic distance in one hydrogen bonded pair between ***R*-TAE** and ***RS*-TAE**. **k,** Shear deformation model of ***RS*-TAE** crystalline lattices and the photos of its cracking.

To further explain this phenomenon from a molecular level, a typical shear force model is established in the crystal lattice (Figs. 3a-c). Since the main crystal surface is parallel to the plane associated with the (001) Miller index, two crystal lattices perpendicular to the (001) plane were selected as the object of stress analysis. Therefore, the external

shear forces (F), whose cutting direction is parallel to the crystallographic c-axis of the crystal lattice, act on the crystal surface that is along the (001) plane, generating certain shear stresses (τ) in two opposite directions along the c-axis (Fig. 3a). Due to the certain crystal rigidity, the shear stresses would result in certain shear deformation and intense internal strains that force ***R*-TAE** molecules to move apart along the directions that are perpendicular to the cutting forces, resulting high internal energy (Fig. 3b). A traditional molecular crystal usually cracks into pieces along the defect since the crystal lattice cannot sustain and accommodate the high internal energy and strains produced. However, it is precisely due to the presence of chiral carbon atoms that the ***R*-TAE** crystal lattice does not have symmetrical elements such as a glide plane while endowing the 2D hydrogen bonding network with the ability to slip and reconstruct in any direction upon external forces. Hydrogen bonds, as a sacrificial scaffold network, would efficiently dissipate the internal energy, thus leading to an ***R*-TAE** crystal into two intact parts under cropping instead of shattering (Fig. 3c).

We also synthesized the racemic molecule ***RS*-TAE**, which has the same composition and zig-zag hydrogen bonding network as the ***R*-TAE** for a comprehensive comparison. Besides chirality, the crystal stacking structures also differ in ***R*-TAE** and ***RS*-TAE**. The disulfide atoms in the ***R*-TAE** lattice orientate along the same direction while the torsion angles ($\varphi_{C\text{-}S\text{-}S\text{-}C}$) of *P*- and *M*- chirality (axial chirality of disulfide) are significantly distinct (Figs. 3d-f and Supplementary Fig. 9). The lack of enantiomers makes ***R*-TAE** crystallize in the space group $P2_1$ (Monoclinic), resulting in a decrease in unit cell symmetry and an increase in torsion angles of the disulfide bonds. The racemic ***RS*-TAE** crystal, however, belongs to a space group with high symmetry (Monoclinic, $P2_1/c$). The disulfide atoms in the ***RS*-TAE** lattice orientate along the opposite directions while the $\varphi_{C\text{-}S\text{-}S\text{-}C}$ of *P*- and *M*- chirality is the same in both *R* and *S* enantiomers (Figs. 3g-i and Supplementary Fig. 10). The ***RS*-TAE** packing motif is more condensed than ***R*-TAE**, making the crystal more rigid and producing more defects upon external stresses and forces, consistent with the nanoindentation measurements (Supplementary Figs. 11-13). Besides, the ***RS*-TAE** crystal structure

possesses plane and axial symmetry, which endows a higher energy barrier for crystal lattice deformations and the associated hydrogen bonds slipping (Fig. 3g). The atomic distances within a hydrogen-bonded pair in the ***RS*-TAE** are symmetrically equal, whereas in ***R*-TAE** they are asymmetrical and unequal (Fig. 3j). The more robust H-bonds network endows ***RS*-TAE** with an exceptionally high activation energy of thermally stimulated processes, while the slipperiness and reconfigurability of the hydrogen bonds lead to a non-linear activation energy profile for ***R*-TAE**, exhibiting a pronounced deviation from linearity (Supplementary Fig. 14 and Table 1). Computational calculations based on the density functional theory (DFT) showed that the internal cohesive energies of ***R*-TAE** crystals were higher than those of ***RS*-TAE** crystals, enabling ***R*-TAE** crystals tend to be more stable with the higher energy gap (Fig. 3j, Supplementary Table 2 and Figs. 15-16). Consequently, ***RS*-TAE** crystals instantly disintegrate into fragments under cropping or slightly bend (Fig. 3k). Moreover, the single crystal obtained from a single enantiomer *R* bearing the carboxylic acid group (*R*-TA) is also rigid, which tends to crack upon cropping (Supplementary Fig. 17), unraveling the synergistic effects of the chiral carbon atom and the primary amide structure at side chain in the ***R*-TAE** crystals.

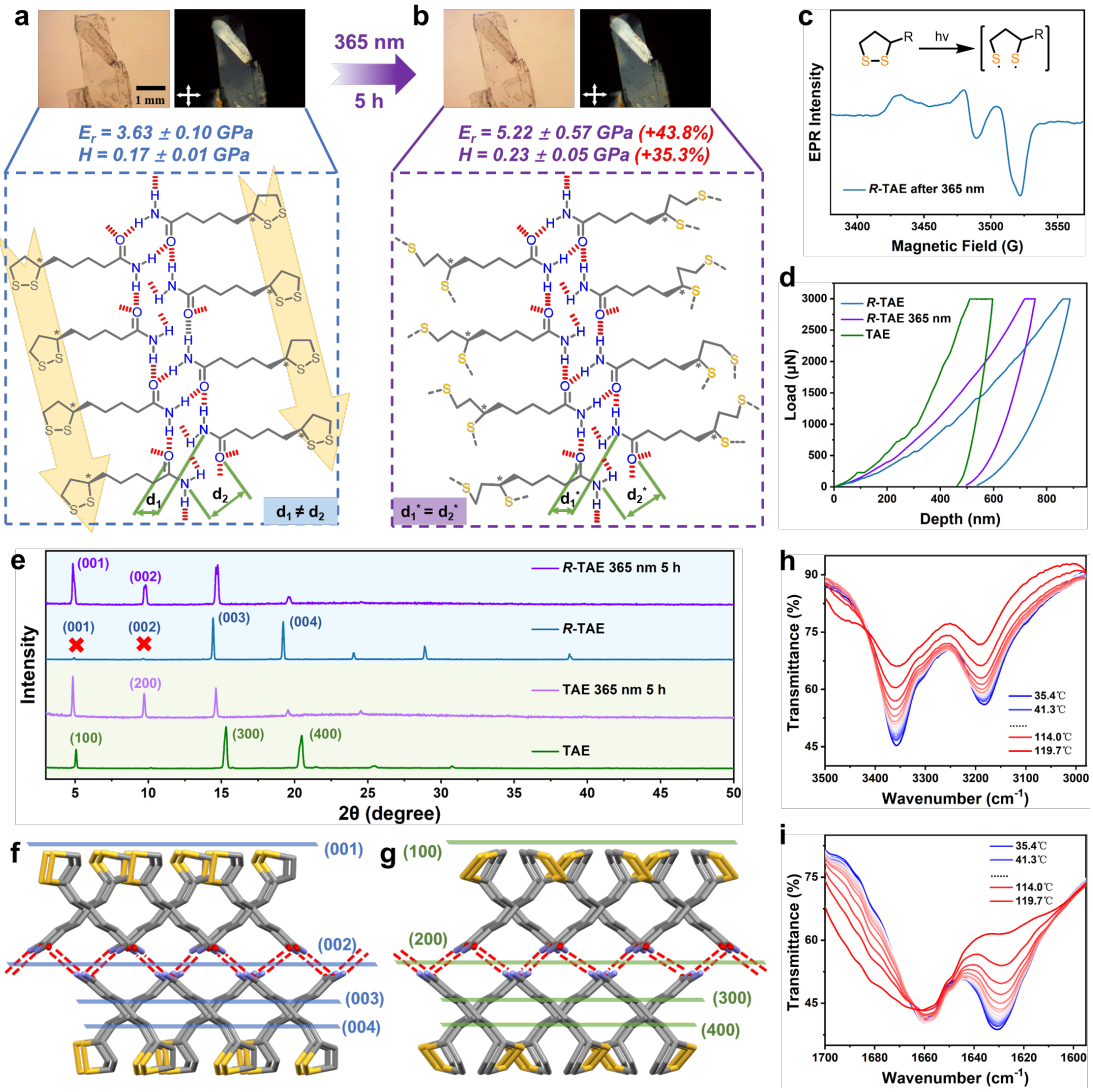

Figure 4. Characterization of radiation-resistant crystalline materials with photo-induced hydrogen bond network reconstruction mechanism. a-b, The photos of radiation resistant capabilities of ***R*-TAE** single crystal and the schematic representation of photo-triggered modulus enhancement. **c,** The electron paramagnetic resonance (EPR) spectrum of ***R*-TAE** powders irradiated by 365 nm light. The inset is the homolysis of 1,2-dithiolane to get disulfide diradicaloid upon ultraviolet (UV) light. **d,** Load-displacement (*P-h*) curves for ***R*-TAE** crystal (blue), ***R*-TAE** upon exposure to 365 nm irradiation crystal (purple), and ***RS*-TAE** crystal (green) at a fixed load (3 mN). **e,** Stacked XRD patterns of ***R*-TAE** (blue) and ***RS*-TAE** (green) crystals and their transformation upon exposure to 365 nm irradiation (purple and pink). **f,** Schematic diagram of crystal planes of ***R*-TAE**. The hydrogen bonds are shown in the red dashed line. **g,** Schematic diagram of crystal planes of ***RS*-TAE**. The hydrogen bonds are shown in the red dashed line. **h-i,** Partial variable temperature infrared spectroscopy (VT-IR) of ***R*-TAE** crystals.

On the other hand, the disulfide bonds in 1,2-dithiolane are prone to form free radicals or intermediates upon external stimuli, such as light or chemicals (acid and based), resulting in ongoing chain reactions to form amorphous structures until adding an end-

capping reagent (Supplementary Fig. 18).[24–29] ***R*-TAE** crystals, however, possess extraordinary stability and durability. Raw ***R*-TAE** single crystals do not experience efflorescence or eroding at ambient conditions after over a year. When exposed to intense ultraviolet (UV) light irradiation (365 nm, 50 mW/cm^2), ***R*-TAE** single crystals undergo a single-crystal-to-single-crystal (SCSC) transformation with overall morphology remaining intact (Figs. 4a-b). The electron paramagnetic resonance (EPR) measurements revealed that the overall hydrogen network might still retained even though disulfide biradicals were observed in the light-illuminated ***R*-TAE** crystals (Fig. 4c). Distinct from the traditional N- or O-centered radicals, the disulfide biradicals were captured by a spin trap of 2,2,6,6-tetramethyl-1-piperidinyloxy (TEMPO) as the spin trap and verified by electrospray ionization mass spectrometry (ESI-MS, Supplementary Fig. 19). Since the primary amide is a neutral group, the sulfonium ions [26] that might be induced by acid catalysis are also not applicable to ***R*-TAE** crystals, allowing excellent resistance to acids. Moreover, the resulting racemic crystals exhibit significant improvements in elastic modulus and hardness by approximately 43.8% and 35.3%, respectively, compared to the initial pristine ***R*-TAE** crystals (Figs. 4a-b, and 4d).

The mechanical properties of ***R*-TAE** and ***RS*-TAE** crystals are also distinctively different (Supplementary Table 3). Given that the molecular structures of the ***RS*-TAE** and ***R*-TAE** are identical, we deduced that they shared the same molecular packing structure after light irradiation. The powder X-ray diffraction (XRD) measurements also verified that the crystalline peaks of the irradiated ***R*-TAE** crystals aligned well with those emanating from the irradiated ***RS*-TAE** crystals (Fig. 4e, purple and pink traces). The schematic diagram of the transformation process is presented in Supplementary Fig. 20. A pristine ***R*-TAE** single crystal exhibits two prominent peaks associated with the (003) and (004) Miller indexes in the XRD patterns due to the stacking of alkyl chains (Figs. 2j and 4e, blue trace). Nevertheless, the patterns lack the crystalline peaks associated with the (001) and (002) Miller indexes because of the asymmetry and slippage between upper and lower crystal lattice layers as well as

unequal distances between each hydrogen bonding site, respectively ($d_1 \neq d_2$, Figs. 3j and 4f). For ***RS*-TAE** crystals, the distances between each hydrogen bonding site are equal (Fig. 3j). A typical ***RS*-TAE** single crystal exhibits a prominent peak associated with the (100) Miller index while does not show a peak associated with the (200) Miller index due to the mutual cancelation from its perfect symmetry (Fig. 4e, green trace). After UV light irradiation, ***RS*-TAE** crystals partially crack as the reorganization of disulfide bonds, allowing the crystalline peak associated (200) index to appear (Figs. 4e, 4g, and Supplementary Figs. 20-22).

In comparison, hydrogen-bonding networks in ***R*-TAE**, which are much more flexible due to the asymmetry effect, can sustain the overall crystal intact after long-period UV exposure. Although the homolysis of disulfide bonds was observed in ***R*-TAE** crystals (Supplementary Figs. 23-24), the sliding of hydrogen bonds might help effectively dissipate substantial photo-generated internal strains of the chemical reaction. Besides, the variable temperature infrared spectroscopy (VT-IR) of ***R*-TAE** crystals also proves its difference from ***RS*-TAE** (Figs. 4h-i and Supplementary Figs. 25-26). Upon irradiation and reorganization of disulfide bonds, the ***R*-TAE** crystalline peaks ascribed to the (001) and (002) indexes appear while the peak ascribed to the (003) index slightly shifts and the peak ascribed to the (004) index diminishes for being too close to the disulfide bonds (Figs. 4e-f and Supplementary Fig. 20). It shows that the hydrogen bond positions are rearranged and the slipping allows for higher interlayer symmetry and order of the H-bonds network after irradiation, resulting in the initially unequal distances ($d_1 \neq d_2$) becoming equal ($d_1^* = d_2^*$) (Figs. 4a-b). We have also demonstrated that this rearrangement is indeed caused by the reorganization of the disulfide bonds, rather than changes in the H-bonds stacking patterns due to the racemization of the sole chiral carbon atom upon light irradiation (Supplementary Figs. 27-28).

Our finding presents the possibility of a direct top-down approach to organic single-crystal shape programming by introducing the chiral asymmetry effect and the steric effect for higher energy dissipation efficiency from a bottom-up strategy. The inherent brittleness and rigidity of molecular crystals inspire us to construct systems of structural

dynamics and energy dynamics from supramolecular chemistry. The modification of the steric effect, the synergistic effects of symmetry loss and high symmetry, and the dynamics of the structure are intertwined in this finding, advancing our knowledge of order and flexibility featuring smartness and sustainability in crystalline materials.

References

1. Liu, T. *et al.* Ultrahigh-printing-speed photoresists for additive manufacturing. *Nat. Nanotechnol.* **19**, 51–57 (2024).
2. Striccoli, M. Photolithography based on nanocrystals. *Science* **357**, 353–354 (2017).
3. Rodgers, P. Top down, bottom up. *Nat. Nanotechnol.* (2006). https://doi.org/10.1038/nnano.2006.87.
4. Jiang, K. *et al.* Mechanical cleavage of non-van der Waals structures towards two-dimensional crystals. *Nat. Synth.* **2**, 58–66 (2022).
5. Huang, Y. *et al.* Universal mechanical exfoliation of large-area 2D crystals. *Nat. Commun.* **11**, 2453 (2020).
6. Tominaga, Y. *et al.* Promotion of protein crystal growth by actively switching crystal growth mode via femtosecond laser ablation. *Nat. Photon.* **10**, 723–726 (2016).
7. Pham, P. V. *et al.* Layer-by-layer thinning of two-dimensional materials. *Chem. Soc. Rev.* **53**, 5190–5226 (2024).
8. Huang, H. *et al.* Near-field-regulated ultrafast laser supra-wavelength structuring directly on ultrahard metallic glasses. *Adv. Mater.* **36**, 2405766 (2024).
9. Takahashi, S. *et al.* Direct creation of three-dimensional photonic crystals by a top-down approach. *Nat. Mater.* **8**, 721–725 (2009).
10. Tong, X. *et al.* Breaking the vitrification limitation of monatomic metals. *Nat. Mater.* **23**, 1193–1199 (2024).
11. Zhang, M. *et al.* 3D nanofabrication via chemo-mechanical transformation of nanocrystal/bulk heterostructures. *Adv. Mater.* **30**, 1800233 (2018).
12. Zhang, Y. *et al.* Connected three-dimensional polyhedral frames for programmable liquid processing. *Nat. Chem. Eng.* **1**, 472–482 (2024).
13. Yu, H. *et al.* Top-down fabrication of calcite nanoshoot arrays by crystal dissolution. *Adv. Mater.* **22**, 3181–3184 (2010).
14. Kim, S. *et al.* Work hardening in colloidal crystals. *Nature* **630**, 648–653 (2024).
15. Xu, W. *et al.* Photo-actuators via epitaxial growth of microcrystal arrays in polymer membranes. *Nat. Mater.* **22**, 1152–1159 (2023).
16. Huang, R. *et al.* Elastic self-doping organic single crystals exhibiting flexible optical waveguide and amplified spontaneous emission. *Adv. Mater.* **30**, 1800814 (2018).
17. Li, W. *et al.* Ultrastrong MXene film induced by sequential bridging with liquid metal. *Science* **385**, 62–68 (2024).

18. Wang, S. *et al.* Electrochemical molecular intercalation and exfoliation of solution-processable two-dimensional crystals. *Nat. Protoc.* **18**, 2814–2837 (2023).
19. Marshall, C. R. *et al.* Size-dependent properties of solution-processable conductive MOF nanocrystals. *J. Am. Chem. Soc.* **144**, 5784–5794 (2022).
20. Thompson, A. J. *et al.* Elastically flexible molecular crystals. *Chem. Soc. Rev.* **50**, 11725–11740 (2021).
21. Takamizawa, S. *et al.* Superplasticity in an organic crystal. *Nat. Commun.* **9**, 3984 (2018).
22. Flack, H. D. Chiral and achiral crystal structures. *Helv. Chim. Acta* **86**, 905–921 (2003).
23. Rekis, T. *et al.* Single enantiomer's urge to crystallize in centrosymmetric space groups: solid solutions of phenylpiracetam. *Cryst. Growth Des.* **17**, 1411–1418 (2017).
24. Barltrop, J. A. *et al.* The chemistry of 1,2-dithiolane (trimethylene disulfide) as a model for the primary quantum conversion act in photosynthesis[1a]. *J. Am. Chem. Soc.* **76**, 4348–4367 (1954).
25. Endo, K. *et al.* Synthesis and characterization of poly(1,2-dithiane). *Macromolecules* **37**, 3143–3150 (2004).
26. Wang, B.-S. *et al.* Acid-catalyzed disulfide-mediated reversible polymerization for recyclable dynamic covalent materials. *Angew. Chem. Int. Ed.* **62**, e202215329 (2023).
27. Zhang, Q. *et al.* Dual closed-loop chemical recycling of synthetic polymers by intrinsically reconfigurable poly(disulfides). *Matter* **4**, 1352–1364 (2021).
28. Zhang, Q. *et al.* Assembling a natural small molecule into a supramolecular network with high structural order and dynamic functions. *J. Am. Chem. Soc.* **141**, 12804–12814 (2019).
29. Nelson, B. R. *et al.* Photoinduced dithiolane crosslinking for multiresponsive dynamic hydrogels. *Adv. Mater.* **36**, 2211209 (2024).

Methods

The materials and the synthesis, isolation, and characterization of ***R*-TAE** and ***RS*-TAE**, photographs, transmission electron microscope, thermal gravimetric analysis, differential scanning calorimetry, electronic spray ionization mass spectra, and density functional theory calculations are fully described in the Supplementary methods.

Single Crystals Preparation

***R*-TAE** monomers were first dissolved in chloroform and filtered to remove possible tiny particles. Then transfer to a clean bottle and carefully and slowly add an equal volume of dichloromethane as a buffer layer, and a yellow and colorless two-phase layered liquid can be seen. Finally, carefully and slowly, twice the volume of cyclohexane as a poor solvent is added, and it is placed in the refrigerator to diffuse and evaporate slowly to obtain flaky transparent crystals. The volume ratio of the solution, buffer layer, and poor solvent layer should be 1:1:2, otherwise it will be difficult to obtain a flat and transparent crystal film.

***RS*-TAE** monomers were dissolved in a 1:1 mixed solvent of dichloromethane and acetonitrile. Then, it slowly evaporated at room temperature in a dark place to obtain yellow needle-like crystals.

Single crystal X-ray diffraction (SCXRD) measurement

Single crystal X-ray diffraction (SCXRD) data were collected on a Bruker D8 VENTURE Metaljet diffractometer equipped with a PHOTON III M28 detector and operated at 50 kV, 40 mA to generate Ga-Kα radiation (λ = 1.34139 Å). Single crystal X-ray diffraction (SCXRD) data were collected on a Bruker D8 VENTURE diffractometer equipped with a PHOTON 100 CMOS detector and operated at 50 kV, 1 mA to generate Mo-Kα radiation (λ = 0.71073 Å).

Optical microscope and cross-polarized microscope imaging

Optical microscope images were taken with a microscope equipped with a CCD camera (Teelen TL3201-LED) and cross-polarized microscope images were taken with a microscope equipped with a polarizer (Leica DM750).

Scanning electron microscopy (SEM) measurements

The crystals were stuck to a piece of carbon tape that was then fixed on an SEM stub. The SEM stub was then placed in a low vacuum coater (Leica EM ACE200) and coated

with Au for 90 s (about 6 nm) to improve the sample conductivity. The SEM (Helios G4 UC) imaged the sample using a 2 kV electron beam with the Everhart−Thornley SE detector (ETD) and Elstar in-lens SE/BSE detector (TLD-SE).

XRD and Mirco-XRD measurements

X-ray diffraction (XRD) patterns were obtained on a rotating anode X-ray powder diffractometer (18KW/D/Max2550VB/PC) equipped with a copper target 18KW (450mA), a fully automated curved (plate) crystal graphite monochromator, and a programmed variable slit system with a step size = 0.02°.

Mirco-XRD patterns were collected on an X-ray powder diffractometer (Rigaku SmartLab SE) equipped with a copper target 18KW (450mA). The sample holder stage was fixed horizontally, and the detector (divergence slit = 0.50 mm without monochromator) rotated over the sample with scanning rate = 4°/min.

Electron paramagnetic resonance (EPR) measurement

Electron paramagnetic resonance (EPR) was performed on Electro-Spin Resonance Spectrometer (Brüker 100G-18KG/EMX-8/2.7) by using solid powder. Experimental parameters are provided as follows: modulation amplitude = 2.00 G, modulation frequency = 100.00 kHz, receiver harmonic = 1, microwave power = 2.016 mW, and microwave frequency = 9.877 GHz.

Nanoindentation measurement

Nanoindentation measurements were performed with a Bruker Hysitron TI980 nanoindenter equipped with a Berkovich diamond indenter. A maximum load value of 3 mN was applied, and a loading/unloading rate of 0.6 mN s^{-1} was used for all of the experiments. The holding time at the maximum load was set to be 2 s.

Variable temperature infrared spectra (VT-IR) measurement

Variable temperature infrared spectra were performed on Nicolet™ iS50 FT-IR Spectrometer by potassium bromide pellet (KBr, spectral grade) with the heating rate = 4°C /min.

Data availability

Data availability Data supporting the findings of this investigation are available from the manuscript and its Supplementary Information. Crystallographic data for the

structures reported have been deposited at the Cambridge Crystallographic Data Centre (CCDC) under deposition numbers 2377862 (***R*-TAE**), 2348912 (***RS*-TAE**), 2356250 (***R*-TA**) and 2348914 (**TA**). Copies of the data can be obtained free of charge via https://www.ccdc.cam.ac.uk/structures/. Supplementary videos are provided with this paper.

Acknowledgments

This work was supported by the National Natural Science Foundation of China (22025503, 22220102004), Science and Technology Commission of Shanghai Municipality (24DX1400200), the Innovation Program of Shanghai Municipal Education Commission (2023ZKZD40), the Programme of Introducing Talents of Discipline to Universities (grant no. B16017) and the Fundamental Research Funds for the Central Universities. We thank the technicians at Shenzhen Huasuan Technology for their assistance with the theoretical calculations.

Author contributions

H.-Y.L. conceived the project. F.T. and D.-H.Q. supervised the research. H.-Y.L., L.L. carried out the synthesis, characterizations, and data acquisition. C.Z. provides theoretical and computational help. H.-Y.L., F.T., C.Y., Q.Z., H.T., B.L.F., and D.-H.Q. analyzed the data and wrote the manuscript. All authors discussed the results and commented on the manuscript.

Competing interests

The authors declare no competing interests.

Correspondence and requests for materials should be addressed to Ben L. Feringa, Fei Tong, or Da-Hui Qu.